JOURNAL OF GEOPHYSICAL RESEARCH, VOL. 93, NO. C8, PAGES 9281–9294, AUGUST 15, 1988

Specular Point Scattering Contribution to the Mean Synthetic Aperture Radar Image of the Ocean Surface

DALE P. WINEBRENNER

Polar Science Center, Applied Physics Laboratory, University of Washington, Seattle

KLAUS HASSELMANN

Max-Planck-Institut fuer Meteorologie, Hamburg, Federal Republic of Germany

In general, the return signal scattered from the ocean surface used to form synthetic aperture radar (SAR) images contains contributions from at least two scattering mechanisms. In addition to resonant Bragg-type scattering, specular point scattering becomes important as the angle of incidence becomes small ($\lesssim 20°$). In this paper we include the specular point rough surface scattering mechanism in a model for the mean SAR image of the ocean surface and examine the effects of this scattering mechanism theoretically. We find that the complete mean SAR intensity image consists of a sum of images due to specular point scattering and Bragg-type resonant scattering. Because surface specular points have a short coherence time and move with considerable velocities, the contribution to the mean image due to these scatterers is of low azimuthal resolution and is displaced from the actual sea surface, typically by several SAR resolution cells. The bandwidth of this image can easily exceed the bandwidth of a typical SAR processor, leading to a loss of mean image intensity. The local backscatter cross-section modulation is strong and nonlinear in the slope of the longwave field in the SAR range direction. At small incidence angles, this causes the specular point return from wave slopes tipped toward the SAR to become much brighter than the Bragg-scattering return. Taken together, these effects are capable of producing azimuthally oriented streaks in SAR images, such as have been observed by Seasat. We present numerical estimates of coherence time, azimuthal displacement, cross-section modulation, etc., computed using the parameters of the Seasat and shuttle imaging radar-B SARs as well as typical parameters for an airborne X band SAR.

1. INTRODUCTION

There has been considerable recent interest in the imaging of the ocean surface by synthetic aperture radar (SAR) operated from airborne and spaceborne platforms, and in the relation of this imaging to the actual ocean surface. Several theories have been given relating the image to the ocean surface [*Alpers and Rufenach*, 1979; *Swift and Wilson*, 1979; *Valenzuela*, 1980; *Jain*, 1981; *Harger*, 1984; *Hasselmann et al.*, 1985].

In particular, a reasonably complete theory to which a substantial number of investigators subscribe has recently been described by *Hasselmann et al.* [1985]. Although the theory was formulated generally for arbitrary spatially decorrelated scattering mechanisms, the only rough surface scattering mechanism considered explicitly was Bragg-type resonance scattering from short gravity and capillary waves. A few comparisons of this theory with data in which the SAR incidence angle is greater than or roughly equal to 20° have been made [*Lyzenga et al.*, 1985; *Alpers et al.*, 1986]. Although many more comparisons are certainly needed, agreement of this theory with the data so far is promising.

However, according to the so-called two-scale or composite roughness surface scattering theory on which SAR imaging theory is based, the return signal from the ocean surface contains contributions both from Bragg scattering and from specular point scattering [*Brown*, 1978; *Valenzuela*, 1978]. In particular, the specular point contribution to the return signal becomes comparable to the Bragg-type contribution for a typical ocean surface when the angle of incidence becomes less than approximately 20°. Spaceborne SARs such as those on Seasat and the shuttle imaging radar–B (SIR-B) mission have operated in this range of incidence angles, and the SIR-C SAR will also be capable of operating in this range. It appears that specular point scattering may play a role in SAR imaging of steep, wind-driven waves and of more complex ocean scenes involving, for example, ocean fronts and ship wakes. In particular, azimuthal streaks observed in some Seasat images of high wind areas [*Jenkins et al.*, 1984] and streaks reported in observations from the Marsen experiment [cf. *Hasselmann et al.*, 1985] are at least qualitatively consistent with a wide bandwidth scattering mechanism such as specular point scattering. Furthermore, scatterometer observations and analysis by *Donelan and Pierson* [1987] and by *Kwoh and Lake* [1984] indicate that specular point scattering may contribute strongly to the signal backscattered from the ocean even at angles of incidence larger than 20° for high winds. Thus we are motivated to consider the effects of this scattering mechanism on SAR ocean surface imaging.

The purpose of this paper is to theoretically include the specular point scattering mechanism in a model for the mean SAR image of the ocean surface. This inclusion is simply a first step and provides the theoretical basis for Monte Carlo simulation of the SAR ocean surface image including specular point effects. Such simulation can then be used for a careful comparison of the complete imaging model with data. We begin with the fundamental model of the SAR imaging process given by *Hasselmann et al.* [1985] (section 2). In this model, the surface reflectivity variance spectrum (or RVS, defined below), is closely related to the mean image under the so-called spatial whiteness assumption. We make explicit use of this latter assumption. Using the composite roughness scatter-

Paper number 8C0297.
0148-0227/88/008C-0297$05.00

ing model, we obtain the full RVS as a sum of two terms, one due to Bragg scattering and the other due to specular point scattering. The SAR imaging model introduces a decomposition of the ocean wave field into two parts. The first part consists of ocean wave spectral components with short spatial and/or temporal scales such that they cannot be explicitly imaged by the SAR (i.e., subresolution-scale components). These wave components and scattering from surface roughness due to them must be treated stochastically. Longer wave components (i.e., long waves) may be treated deterministically for a given scene. The results derived in this paper concern the mean SAR image, averaged over the ensemble of realizations of subresolution-scale roughness, as opposed to a SAR image of an individual specular point. In addition, we will consider only the mean from a single look. Thus noncoherent brightness modulation of the image from look to look of the type considered by *Raney and Vachon* [1988] does not arise. For spaceborne SARs, which are our primary interest here, noncoherent brightness modulation effects within a single look are evidently not significant. We first consider the case in which no longwave field is present (section 3) and then remove this restriction (section 4).

We find that the specular point scattering image is characterized by a large Doppler broadening, i.e., by a short coherence time (≈ 0.03 s at X band), and by a relatively large Doppler shift in its reflectivity variance spectrum. Thus the image due to this scattering mechanism is of low azimuthal resolution and is typically displaced by several resolution cells from the true ocean surface. The bandwidth of this image can easily exceed the bandwidth of a typical SAR processor, leading to a loss of mean image intensity. The displacement and bandwidth of the image, however, depend strongly on the SAR azimuth direction relative to the mean wave propagation direction, with the greatest effect for range-traveling waves. The displacement and bandwidth of the image of a particular resolution cell also depend to a lesser degree on its position within the longwave field. We find that the local backscatter cross-section modulation in the specular point scattering contribution is strong and nonlinear in the slope of the longwave field in the SAR range direction. At small incidence angle, this effect causes the specular point return from the slopes of range-traveling waves tipped toward the SAR to become much brighter than the Bragg scattering return.

At incidence angles where specular point scattering is intermittent, the combination of these effects would produce azimuthally aligned streaks superimposed on the Bragg-scattering image. Their length is determined primarily by the degraded azimuthal resolution, which in turn depends on the coherence time of specular point scattering. Their brightness and prevalance is determined by the slope spectrum of subresolution-scale roughness, longwave slope, SAR incidence angle, and SAR bandwidth.

We have computed representative numerical results for coherence time, the associated degradation of azimuthal resolution, and azimuthal image displacement using two simple approximations for the ocean wave spectrum and the parameters of the Seasat and SIR-B spaceborne SARs and of a typical airborne X band SAR. We have also computed representative numerical values for the cross-section modulation using the SIR-B parameters. These results, presented in sections 3 and 4, provide first estimates of the magnitudes of the effects discussed. The computed degradation of azimuthal resolution of the Seasat SAR provides a first estimate of the length of streaks which could be expected in images from this SAR. This estimate is shown in section 4 to be in good agreement with the observed lengths of streaks in the Seasat image presented by *Jenkins et al.* [1984]. Finally, the conclusions are summarized in section 5.

2. Theoretical Background

We consider a SAR system in which the Doppler spectrum of the imaged scene is adequately sampled, allowing us to treat the received signal as a continuous function of platform position or, equivalently, time. We have rechecked and verified this assumption for a few representative systems (Seasat, SIR-B, and typical aircraft SARs) in view of the rather large bandwidth of the specular point scattering mechanism to be discussed here. Furthermore, we assume that effects of range-azimuth coupling, range curvature, and range walk are negligible or may be corrected. Conditions under which these assumptions hold have been thoroughly discussed by a number of authors [cf. *Harger*, 1970; *Tomiyasu*, 1978; *Ulaby et al.*, 1982].

Figure 1 shows the physical situation with the SAR platform traveling along the x axis at altitude h above the mean plane of the imaged surface. The latter plane is taken to be $z = 0$. The SAR azimuth direction is the $\hat{x}$ direction, while the range direction is the $\hat{y}$ direction. We assume that the real aperture antenna of the SAR is pointed perpendicular to the direction of platform travel.

The rough surface constituting the scene to be imaged is regarded as a collection of scattering regions. The projection of each scattering region into the plane of the mean surface has dimensions in the SAR range and azimuth directions given approximately by twice the theoretical SAR range and azimuth resolution lengths, respectively, and has total area A. The choice of these length scales is discussed further below.

Referring to Figure 2, let $E_p^i(\hat{i}) \exp(-i\omega_o t)$ be the SAR illumination field with polarization $\hat{p}$ incident on a scattering region centered at (x', y'). We assume that $E_p^i(\hat{i})$ may be considered to be a plane wave incident from the direction $\hat{i}$, at

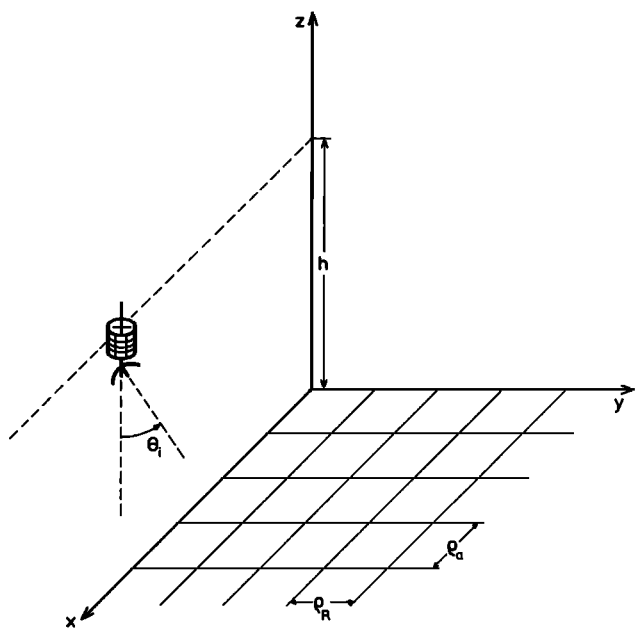

Fig. 1. SAR geometry. Notation is as follows: ρ_R and ρ_a are SAR range and nominal azimuthal resolutions, respectively, the SAR platform altitude is h, and the nominal angle of incidence is θ_i.

least over individual scattering regions. The local polar and azimuthal angles of incidence are θ_i and ϕ_i, respectively. According to our previous discussion (compare Figure 1), $\hat{\imath}$ lies in the y-z plane, and thus $\phi_i = -(\pi/2)$. For the moment, though, we do not restrict these quantities. Range resolution in SAR systems is obtained by using effectively short pulses in which a range of temporal frequencies are present. However, we assume that the response of the rough surface varies negligibly over the range of frequencies (bandwidth) present in the incident pulse. Thus we need consider the response of the rough surface only at the single frequency $\omega_o = ck$, where $k = 2\pi/\lambda$ is the wave number corresponding to the center frequency at which the SAR operates.

In the far field of the scattering region, the scattered field at frequency ω_o scattered in the direction $\hat{o}$ with polarization $\hat{p}'$ may be written [*Ishimaru*, 1978]

$$\hat{p}' \cdot \bar{E}^{\text{scat}}(\hat{o}, t) = \frac{\exp[ikR_o - i\omega_o t]}{4\pi R_o} E_{p'}{}^{s}(\hat{o}, t)\hat{p}' \tag{1}$$

where R_o is the range from the scattering region and where, in general, $E_{p'}{}^{s}(\hat{o}, t)$ depends on time because of the motion of the rough surface. Each scattering region is characterized by a complex reflectivity density ψ, relating the local incident and far field scattered fields at a given frequency according to

$$E_{p'}{}^{s}(\hat{o}, t) = \psi(\hat{o}, \hat{\imath}, \hat{p}, \hat{p}', \omega_o, x', y', t)E_p{}^{i}(\hat{\imath}) \tag{2}$$

For brevity, we suppress the dependence of ψ on $\hat{o}$, $\hat{\imath}$, $\hat{p}$, $\hat{p}'$, and ω_o. In this work we are interested exclusively in backscatter $\hat{o} = -\hat{\imath}$. Common choices for $\hat{p}$ and $\hat{p}'$ correspond to the usual horizontal and vertical polarization directions $\hat{h}$ and $\hat{v}$, though $\hat{p}$ and $\hat{p}'$ need not be in the same direction.

$$\hat{h} = \hat{x}\sin\phi_i - \hat{y}\cos\phi_i \tag{3a}$$

$$\hat{v} = -\hat{x}\cos\theta_i\cos\phi_i - \hat{y}\cos\theta_i\sin\phi_i + \hat{z}\sin\theta_i \tag{3b}$$

The reflectivity density is normalized such that

$$\begin{aligned}\langle\psi(x', y', t_1)\psi^*(x'', y'', t_2)\rangle &= \sigma_t(x', y', t_1, t_2)\delta(x' - x'')\delta(y' - y'') \\ &= \sigma(x', y')\Psi(x', y', t_C, t_D)\delta(x' - x'')\delta(y' - y'')\end{aligned} \tag{4}$$

where

$$t_C = \tfrac{1}{2}(t_1 + t_2) \qquad t_D = t_2 - t_1$$

and where σ_t is simply the time-correlated backscattering cross-section of the scattering region [cf. *Ishimaru*, 1978]. We assume that this cross section may be written as a product of its value at zero lag t_D, σ, and a new function Ψ describing its variation with time.

A significant simplification in the SAR imaging theory results if it may be assumed that the reflectivity density of distinct scattering regions is spatially uncorrelated for all time lags t_D. This is the so-called spatial whiteness assumption and is expressed by the delta functions in (4). We note that spatial whiteness does not require independence of the reflectivity density from distinct scattering regions but requires only a lack of phase correlation (and therefore complex amplitude) on the length scale of the SAR resolution lengths. This assumption is fully consistent with existing theory and experimental results and will be made throughout the present study. A more detailed discussion on this point is given by *Hasselmann et al.* [1985].

Using the whiteness relation, the equations describing SAR

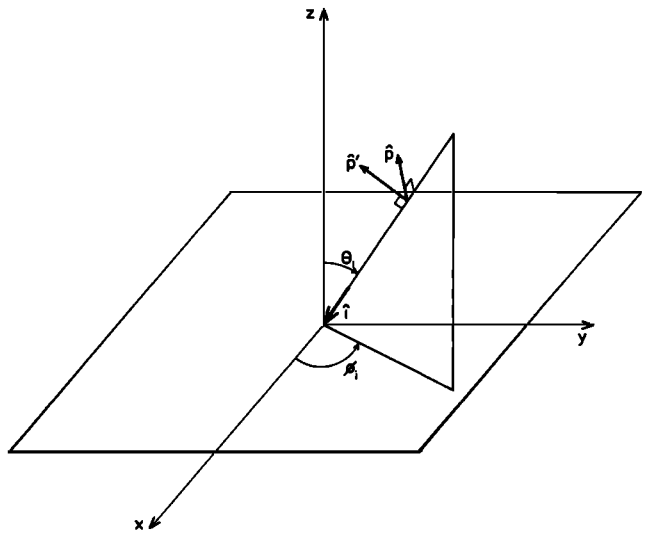

Fig. 2. Radiation incident on a scattering region. Notation is as follows: $\hat{\imath}$ is unit vector in the direction of incidence specified by polar and azimuthal angles θ_i and ϕ_i, respectively: $\hat{p}$ and $\hat{p}'$ are polarization vectors in the plane orthogonal to $\hat{\imath}$.

processing (given in Appendix A), and equations (1)–(4), we arrive then at the following equation for the mean SAR (intensity) image:

$$\langle I(x, y)\rangle = \int dx' \int dy'\sigma(x', y')|T_R(y - y', y, h)|^2 \cdot\Psi\left(x', y', T_i, T_s, \frac{2kV}{R_o}(x - x')\right) \tag{5}$$

where x and y are image coordinates, T_R is the SAR impulse response in the range direction, Ψ is the reflectivity variance spectrum given by

$$\begin{aligned}\Psi(x', y', T_i, T_s, \omega) &= V^2 \int dt_C \int dt_D \\ &\cdot\exp[-i\omega t_D]\Psi(x', y', t_C, t_D) \\ &\cdot\exp\left\{-4\left[\frac{t_C{}^2}{T_i{}^2} + \frac{(t_C - R_o\omega/2kV)^2}{T_s{}^2}\right] - t_D{}^2\left(\frac{1}{T_i{}^2} + \frac{1}{T_s{}^2}\right)\right\}\end{aligned} \tag{6}$$

T_i is the SAR integration time, and T_s is an analogous time which determines the SAR processor bandwidth according to equation (A6). (We have explicitly included the finite SAR processor bandwidth in order to make clear the effect of the large signal bandwidth in this problem.) The statistical scattering properties of the ocean surface evidently enter the computation of the mean image via the time-correlated backscatter cross section.

We shall consider a scattering region within which, depending on the angle of incidence, both Bragg-type and specular point scattering may contribute to the scattered field. It is rare for "scatterers" of either scattering mechanism to propagate from one scattering region to another over the course of a typical SAR integration time. This is true in the case of the Bragg scattering mechanism because the slightly rough surface patches involved are simply advected with the orbital motion of longer gravity waves [*Alpers and Bruening*, 1986; *Tucker*, 1985] and thus move only short distances during a SAR integration period. Representative numerical results given below (section 3) indicate that while specular points move with con-

siderable speed (roughly the phase speed of short gravity waves), they coherently scatter a signal for only a short time ($\approx$0.1 s at L band to 0.03 s at X band). Thus both types of scattering may be considered as localized within nominal SAR resolution cells.

In computing the cross section, it is necessary to distinguish between surface roughness components of spatial wavelengths longer than the nominal SAR resolution, which may be explicitly imaged by the SAR, and surface roughness on length scales smaller than the nominal resolution. The effect on the imaging process of the latter roughness can be considered only statistically. If energy is present at longer spatial wavelengths, its effect is to tilt, advect, and accelerate the individual scattering regions. These effects can be considered deterministically for a given scene and investigated using simulation and Monte Carlo techniques [*Alpers et al.*, 1986]. In the next section we first consider the backscatter cross section and reflectivity variance spectrum in the absence of waves (i.e., spectral components) longer than the SAR resolution scale. In the following section, we consider the modulation of this fundamental cross section and RVS by the long waves in order to study imaging of these waves.

3. Time-Correlated Cross Section in the Absence of Long Waves

The composite roughness or two-scale model may be used to compute the backscatter cross section of the ocean surface at moderate incidence angles ($\lesssim 60°$) [*Wright*, 1968; *Bass et al.*, 1968; *Hasselmann and Schieler*, 1970; *Brown*, 1978; *Valenzuela*, 1978; *Hasselmann et al.*, 1985]. This model involves a decomposition of the rough surface height into a sum of two heights. The surface roughness spectrum is partitioned at a wave number K_{EMH} depending on the radiation wavelength and properties of the spectrum as shown in Figure 3. Spectral components to the left of the partition define the "large-scale" roughness; the Kirchhoff approximation is used to compute the field which would be scattered from this surface alone. A perturbative correction is added to this field which is linear in the surface height of the "small-scale" roughness (i.e., roughness due to spectral components to the right of the partition). The small-scale height variations must be small compared with the radiation wavelength. The resulting expression for the backscattered field is [*Brown*, 1978, 1981; *Stogryn*, 1967]

$$E_{p'}(-\hat{\imath}, t) = \frac{-2i\varepsilon_{pp'}F(0)\,|E^i|}{\cos\theta_i}\int d^2R'' \cdot \exp\,[2i\bar{K}_i\cdot\bar{R}'' - 2ik_z(\bar{K}_i)h_L(\bar{R}'', t)] + 4k^2\,|E^i|\int d^2R''\Gamma_{pp'}(\nabla h_L(\bar{R}'', t))h_s(\bar{R}'', t) \cdot \exp\,[2i\bar{K}_i\cdot\bar{R}'' - 2ik_z(\bar{K}_i)h_L(\bar{R}'', t)] \quad (7a)$$

Here,

$$\begin{aligned} \varepsilon_{pp'} &= -1 \qquad \hat{p} = \hat{p}' = \hat{h} \\ \varepsilon_{pp'} &= 0 \qquad \hat{p} \neq \hat{p} \\ \varepsilon_{pp'} &= 1 \qquad \hat{p} = \hat{p}' = \hat{v} \end{aligned} \quad (7b)$$

$F(0)$ is the Fresnel power reflection coefficient for the scattering medium evaluated at normal incidence (which is the same for either polarization), $h_L(\bar{R}'', t)$ is the evaluation of the large-scale surface at $\bar{R}'' = (x'', y'')$, $h_S(\bar{R}'', t)$ is the elevation of the small-scale surface, and $\Gamma_{pp'}(\nabla h(\bar{R}'', t))$ is a rather complicated

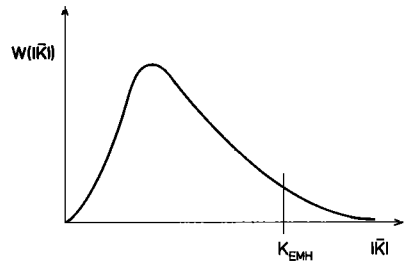

Fig. 3. Partition of the ocean surface wave spectrum at K_{EMH} for two-scale scattering theory (EMH stands for "electromagnetic-hydrodynamic").

function of the large-scale surface slopes, polarization of the incident and scattered waves, and dielectric properties of the scattering surface. The integration over $\bar{R}''$ ranges over the scattering region centered at (x', y'), and $\bar{K}_i$ and $k_z(\bar{K}_i)$ are defined by

$$\begin{aligned} \bar{K}_i &= -k(\hat{x}\sin\theta_i\cos\phi_i + \hat{y}\sin\theta_i\sin\phi_i) \\ k_z(\bar{K}_i) &= k\cos\theta_i \end{aligned} \quad (7c)$$

To obtain this result for a time-varying rough surface, we have also used the fact that the Helmholz equation applies to electromagnetic scattering from natural moving surfaces in virtually all practical situations [*Kleinman and Mack*, 1979; *Cooper*, 1980].

The expression for the backscatter cross section appearing in (4) is then

$$\begin{aligned} \sigma_t(x', y', t_1, t_2) = \int d^2(R_2 - R_1)\exp\,[2i\bar{K}_i\cdot(\bar{R}_2 - \bar{R}_1)] \\ \cdot\Big\langle \exp\,\{-2ik_z(\bar{K}_i)[h_L(\bar{R}_2, t_2) - h_L(\bar{R}_1, t_1)]\} \\ \cdot\Big\{\frac{k^2\,|F(0)|^2}{\cos^2\theta_i} + 4k^4h_s(\bar{R}_1, t_1)h_s(\bar{R}_2, t_2) \\ \cdot\Gamma_{pp'}(\nabla h_L(\bar{R}_1, t_1))\Gamma_{pp'}{}^*(\nabla h_L(\bar{R}_2, t_2)) \\ + 2RE\Big[\frac{2ik^3F(0)}{\cos\theta_i}h_s(\bar{R}_2, t_2)\Gamma_{pp'}(\nabla h_L(\bar{R}_1, t_1))\Big]\Big\}\Big\rangle \end{aligned} \quad (8)$$

where $\bar{R}_2$ and $\bar{R}_1$ are the horizontal positions of points on the rough surface. The first two terms of the integrand in this expression are due to physical optics scattering and resonant Bragg scattering (modulated by the large-scale surface slopes), respectively. The third term depends on a mixed moment of the large- and small-scale surface heights. If the sea surface heights possessed a truly Gaussian distribution, this term would be identically zero, since in that case h_s may be considered a zero-mean random process independent of h_L. However, the actual distribution of sea surface heights is nearly but not quite Gaussian [cf. *Phillips*, 1977], and so this third term requires further consideration.

That this term is still negligible even for a weakly non-Gaussian surface may be seen by the following argument. The averaging over ensembles of rough ocean surfaces may be considered as a two-step sequence. First, averaging over the small-scale surface is carried out conditionally for a given realization of the large-scale surface, after which averaging over the ensemble of large-scale surfaces is performed. While the variance of h_s is certainly larger in certain regions on the

large-scale surface because of the effects of wind and hydrodynamic modulation, the uniform phase distribution of the short spectral components of which h_s consists is not affected by the long waves, at least according to weak interaction theories [*Alpers and Hasselmann*, 1978; *Keller and Wright*, 1975; *Longuet-Higgins and Stewart*, 1964]. Thus h_s can be modeled as a zero-mean perturbation, approximately as likely to be positive or negative by a given amount at a given point on the large-scale surface. Therefore the average of the term in question is negligible in comparison with the averages of the first two terms in (8). With this simplification, both the time-correlated backscatter cross section and the mean SAR image are seen to consist simply of two components, one due to resonant scattering from small-scale relief, the other due to physical optics type scattering.

As was mentioned in the introduction, the image resulting from the Bragg-type scattering term has already received considerable theoretical attention. Thus we restrict our attention here to the image resulting from the physical optics term in (8),

$$\sigma_t^{po}(x', y', t_1, t_2) = \frac{k^2 |F(0)|^2}{\cos^2 \theta_i} \int d^2(\bar{R}_2 - \bar{R}_1) \cdot \exp [2i\bar{K}_i \cdot (\bar{R}_2 - \bar{R}_1)] \cdot \langle \exp \{-2ik_z(\bar{K}_i)[h_L(\bar{R}_2, t_2) - h_L(\bar{R}_1, t_1)]\} \rangle \quad (9)$$

When considering scattering from the ocean surface at microwave frequencies, it is appropriate to use the high-frequency (i.e., geometric optics) limit of physical optics [*Valenzuela*, 1978]. In this limit, radiation is scattered into a given direction from surface regions (i.e., facets) with slope such that the local specular direction coincides with the scattering direction. Thus, the backscatter cross section is proportional to the joint x and y slope probability density function (PDF) evaluated at the appropriate slopes [*Kodis*, 1966; *Barrick*, 1968*a*, *b*]. Furthermore, a slight extension of the method of *Barrick* [1968*b*] to the case of moving rough surfaces can be used to formally compute the Fourier transform of σ_t with respect to lag, i.e., the Doppler spectrum of frequency variations of the scattered signal about the carrier frequency due to motion of the scattering surface [cf. *Ishimaru*, 1978]. It is shown in Appendix B that this spectrum is simply proportional to the joint PDF of surface derivatives with respect to x, y, and t, evaluated at the x and y slopes corresponding to local specular reflection and at the instantaneous vertical velocity which produces the Doppler shift ω. Suppose we define some appropriate measure of the width of this spectrum in the variable ω. Then this is also a measure of the spread of local vertical velocities of facets with the proper slope for specular reflection and inversely proportional to the coherence time of radiation scattered from the surface.

Although it is the ensemble average behavior of specular points that determines the characteristics of the mean specular point SAR image, there is considerable physical insight to be gained from studies of individual specular point behavior. *Longuet-Higgins* [1960*a*, *b*, *c*] has studied the behavior of specular points on a surface having a Gaussian height distribution and has developed estimates of the mean specular point lifetime. For the ocean surface and incidence angles of roughly 20°, this mean lifetime may be estimated to be of the order of 0.1 s. We will see shortly that the coherence time of radiation scattered from the ocean surface can be considerably shorter than this mean lifetime estimate. However, the reason for this is also clarified by the work of *Longuet-Higgins* [1960*a*], in which it is shown that specular points move along curved (often closed) paths with a highly variable speed. Thus the residual time variability of each scatterer in any reference frame moving with constant velocity is large, and the associated Doppler shift is highly irregular and stochastic in nature. This can cause the coherence time to be shorter than the lifetime of the specular point itself and also accounts for the large Doppler broadening and mean Doppler shift in the reflectivity variance spectrum shown below.

In the case of the sea surface, it is simplest to obtain explicit results using the fact that the large-scale surface heights are (very nearly) Gaussian. In this case,

$$\langle \exp \{-2ik_z(\bar{K}_i)[h_L(\bar{R}_2, t_2) - h_L(\bar{R}_1, t_1)]\} \rangle = \exp \{-4k_z^2(\bar{K}_i)\overline{h_I^2} [1 - C(\bar{R}_D, t_D)]\} \quad (10)$$

where

$$\langle h_L^2(\bar{R}, t) \rangle \equiv \overline{h_I^2}$$
$$\langle h_L(\bar{R}_2, t_2) h_L(\bar{R}_1, t_1) \rangle = \overline{h_I^2} C(\bar{R}_D, t_D)$$
$$\bar{R}_D = \bar{R}_2 - \bar{R}_1 \qquad t_D = t_2 - t_1$$

where C is the normalized correlation function of the large-scale surface height.

In the high-frequency limit, the integrand in (9) is highly peaked about $|\bar{R}_D| = 0$. For a differentiable surface (as the large-scale surface must be in order to apply physical optics), the normalized correlation function may be approximated for short lags $\bar{R}_D = (x_D, y_D)$ by

$$C(x_D, y_D, t_D) \approx 1 + C_{xx}x_D^2 + C_{yy}y_D^2 + C_{tt}t_D^2 + C_{xt}x_D t_D + C_{yt}y_D t_D + C_{xy}x_D y_D \quad (11)$$

where $C_{\alpha\alpha} < 0$ for $\alpha = x$, y, or t, and the other coefficients may be positive, negative, or zero. These coefficients are simply related to derivatives of the normalized correlation function evaluated at zero lag,

$$C_{\alpha\alpha} = \frac{1}{2} \frac{\partial^2 C}{\partial \alpha^2}\bigg|_{x_D = y_D = t_D = 0} \qquad \alpha = x, y, \text{ or } t$$
$$C_{\alpha\beta} = \frac{\partial^2 C}{\partial \alpha \partial \beta}\bigg|_{x_D = y_D = t_D = 0} \qquad \alpha \neq \beta$$

The integration limits in (9) may be extended to infinity with negligible error so long as the scattering region contains several correlation lengths of the surface roughness. The indicated integrations may then be performed immediately, yielding

$$\sigma_t(x', y', t_1, t_2) = \sigma(x', y') \exp \left[-\frac{t_D^2}{\tau_s^2} + i\omega_D t_D \right] \quad (12)$$

where

$$\sigma(x', y') = [2 \cos^4 \theta_i \overline{h_I^2} (|C_{xx}||C_{yy}| + \tfrac{1}{4}C_{xy}^2)^{1/2}]^{-1} \cdot \exp \left\{ -\left[2k_z^2(\bar{K}_i)\overline{h_I^2} \left(1 - \frac{C_{xy}^2}{4|C_{xx}||C_{yy}|} \right) \right]^{-1} \cdot \left[\frac{K_{ix}^2}{|C_{xx}|} + \frac{K_{iy}^2}{|C_{yy}|} + K_{ix}K_{iy} \frac{C_{xy}}{|C_{xx}||C_{yy}|} \right] \right\} \quad (13)$$

$$\tau_s = [(2\overline{h_I^2})^{1/2} k_z(\bar{K}_i)]^{-1} \left\{ |C_{tt}| - \frac{1}{4}\left(1 - \frac{C_{xt}^2}{4|C_{xx}||C_{yy}|}\right)^{-1} \cdot \left[\frac{C_{xt}^2}{|C_{xx}|} + \frac{C_{yt}^2}{|C_{yy}|} + \frac{C_{xt}C_{xy}C_{yt}}{|C_{xx}||C_{yy}|}\right]\right\}^{1/2} \quad (14)$$

$$\omega_D = \left(1 - \frac{C_{xy}^2}{4|C_{xx}||C_{yy}|}\right)^{-1} \left[K_{ix}\left(\frac{C_{xt}}{|C_{xx}|} + \frac{C_{yt}C_{xy}}{2|C_{xx}||C_{yy}|}\right) + K_{iy}\left(\frac{C_{yt}}{|C_{yy}|} + \frac{C_{xt}C_{xy}}{2|C_{xx}||C_{yy}|}\right)\right] \quad (15)$$

Using (7*c*), these quantities may be expressed simply in terms of the incidence angles θ_i and ϕ_i and the SAR radiation wave number k. Note that the form of (12) agrees with that assumed in (4). A physical explanation of each term in (12) will be given momentarily.

The indicated derivatives of the normalized correlation function at zero lag may be computed as moments of the surface roughness spectrum through the relations

$$C_{xx} = (2\pi)^{-2} \int d^2K\, K_x^2 W(\bar{K}) \quad (16a)$$

$$C_{yy} = (2\pi)^{-2} \int d^2K\, K_y^2 W(\bar{K}) \quad (16b)$$

$$C_{tt} = g(2\pi)^{-2} \int d^2K\, |\bar{K}| W(\bar{K}) \quad (16c)$$

$$C_{xy} = 2(2\pi)^{-2} \int d^2K\, K_x K_y W(\bar{K}) \quad (16d)$$

$$C_{xt} = 2g^{1/2}(2\pi)^{-2} \int d^2K\, K_x |\bar{K}|^{1/2} W(\bar{K}) \quad (16e)$$

$$C_{yt} = 2g^{1/2}(2\pi)^{-2} \int d^2K\, K_y |\bar{K}|^{1/2} W(\bar{K}) \quad (16f)$$

where g is the acceleration due to gravity, $\bar{K} = K_x\hat{x} + K_y\hat{y}$, and $dK = dK_x\, dK_y$. The integrations in (16*a*)–(16*f*) extend over all $\bar{K}$ in the range $K_{SAR} < |\bar{K}| < K_{EMH}$. The lower integration limit, K_{SAR}, is defined as the spatial wave number of the shortest-wave spectral component which could conceivably be imaged by the SAR (section 4). In this section we assume that no "long waves," i.e., wave components which may be deterministically imaged, are present, so that the spectrum W is assumed to have no energy at wave numbers of magnitude smaller than K_{SAR}. In the next section, however, this will not be the case. The subscript I in $\overline{h_I^2}$ anticipates the designation of surface roughness due to spectral components in the range $K_{SAR} < |\bar{K}| < K_{EMH}$ as "intermediate-scale" roughness. Note that for convenience, we have normalized the (two-sided) ocean surface roughness spectrum such that

$$1 = 2(2\pi)^{-2} \int_{K_{SAR} < |\bar{K}| < K_{EMH}} d^2K\, W(\bar{K}) \quad (17)$$

in contrast to the more usual oceanographic normalization

$$\overline{h^2} = \text{total mean square wave height} = \int_{\text{all } \bar{K}} d^2K\, W_o(\bar{K})$$

The two spectra are simply related via

$$W_o(\bar{K}) = 2\overline{h_I^2}(2\pi)^{-2} W(\bar{K})$$

The factor $\sigma(x', y')$ in (12) is the geometric optics backscatter cross section for a stationary rough surface. This cross section results from taking a high-frequency limit and is superficially frequency independent (this can be easily checked in (13)). However, $\sigma(x', y')$ is the cross section of the intermediate-scale rough surface consisting of spectral components with magnitude between K_{SAR} and K_{EMH}. Thus it does depend on the system parameters, including radiation wavelength, which determine these spectral partitions. It is this cross section, together with the level of Bragg scattering at small incidence angles, that determines the angular regime in which specular point scattering significantly contributes to the backscattered signal. The quantities $|C_{xx}|$, $|C_{yy}|$, and C_{xy} are proportional to the mean square slopes of intermediate scale roughness in the x (SAR azimuth) direction, the y (SAR range) direction, and the correlation between these slopes, respectively. As the intermediate scale surface slopes grow, $\sigma(x', y')$ becomes broader as function of angle, but its peak value (at vertical incidence) becomes smaller [cf. *Barrick*, 1968*a*]. The correlation between slopes introduces a dependence of the contribution on the directional properties of the roughness relative to the SAR range and azimuth coordinates. The magnitudes of the surface slopes, the directional character of the roughness, and the level of Bragg scattering are related in complicated ways to wind, fetch, currents, atmospheric stability, and other factors. The nature of these dependencies is an active and controversial area of research [for reviews, see *Donelan and Pierson*, 1987; *Plant*, 1982]. As was previously mentioned, specular point scattering is generally considered to be significant only for incidence angles $\lesssim 20°$, but there are indications that it may also contribute at larger angles under some conditions [*Donelan and Pierson*, 1987]. We believe that an attempt to set precise limits on this angular region would be premature as well as beyond the scope of the present investigation. Rather, the present investigation lays the groundwork necessary for such further investigation. Equations (13) and (16*a*)–(16*f*) provide the means to compute $\sigma(x', y')$ once the intermediate-scale wave spectrum is specified.

The time-varying part of the cross section in (12) is simply a signal of constant frequency with Gaussian amplitude modulation. The frequency and temporal width of the modulation depend on the spectral moments given above and thus on the directional quality of the surface wave spectrum. In particular, the moments C_{xt} and C_{yt} are zero in cases where the surface wave spectrum is symmetric about the x (azimuth) and y (range) axes. We refer to this case as a "fully confused sea"; that term as defined here implies that waves propagating in opposite directions have equal energy, and it therefore represents a rather unrealistic limiting case useful for illustrative purposes only. The temporal width τ_s, or so-called coherence time, for a fully confused sea is proportional to $|C_{tt}|^{1/2}$, which in turn is proportional to the intermediate-scale wave orbital velocity. This is consistent with our more general discussion of this quantity earlier. The offset frequency ω_D in this case is zero. Sea surfaces with more directional spectra display longer coherence times. In the limit of a surface with only a single spectral component (i.e., as the spectrum approaches a delta function centered at some K_x, K_y), it is not difficult to show that the frequency ω_D is simply the Doppler frequency resulting from a target with the phase velocity of a monochromatic wave having wave vector $\bar{K}' = K_x'\hat{x} + K_y'\hat{y}$. Finally, note that (14) does not imply that τ_s is simply proportional k^{-1}, since K_{SAR} and K_{EMH}, and thus also C_{xx}, C_{tt}, etc., vary with k. Table 1 presents some representative numerical results for coherence time and Doppler offset and their equivalent

TABLE 1. Representative Numerical Results for Coherence Time and Doppler Offset Frequency

Parameter	Seasat	SIR-B (Orbit 106)	Representative Aircraft SAR (X Band)
λ, cm	23.5	23.5	3
T_i, s	0.62	0.12	1
k, m^{-1}	26.7	26.7	209
K_{SAR}, m^{-1}	0.126	0.165	1.05
K_{EMH}, m^{-1}	4	4	95
θ_i, deg	22	18	25
ρ_a, m	25	38	3
R_o/V, s	130	33	80
$\cos^2(\Phi - \Phi_o/2)$ Spreading Function			
τ_s, s	0.0945	0.107	0.0340
ω_D, Hz	84.1 $\sin\Phi_o$	63.7 $\sin\Phi_o$	215 $\sin\Phi_o$
ρ_a'/ρ_a ($A_R = 0$)	6.64	1.50	29.4
x_D, m	204 $\sin\Phi_o$	39.3 $\sin\Phi_o$	41.1 $\sin\Phi_o$
Isotropic Spreading Function			
τ_s, s	0.0730	0.0818	0.0272
ω_D, Hz	0	0	0
ρ_a'/ρ_a ($A_R = 0$)	8.55	1.78	36.8
x_D, m	0	0	0

image parameters, computed using two simple forms for the ocean surface roughness spectrum and three sets of SAR parameters.

The first spectral form used is a Phillips wind wave spectrum with a frequency independent directionality function. We have taken the peak wave number of the spectrum to be K_{SAR} and the mean wave propagation direction to be Φ_o.

$$W_1(\bar{K}) = W_1(|\bar{K}|, \Phi) = \frac{4\pi}{[(1/K_{SAR}) - (1/K_{EMH})]} |\bar{K}|^{-4} \cos^2\left(\frac{\Phi - \Phi_o}{2}\right) \quad (18)$$

We chose this simple form to provide first estimates of τ_s and ω_D for a fully developed wind sea, both in the present case where we assume that no waves long enough to be deterministically imaged are present, and the in case in the next section where such waves are present.

For comparison, we have also computed τ_s using a Phillips spectrum with isotropic directional distribution (the case of a fully confused sea).

$$W_2(\bar{K}) = W_2(|\bar{K}|) = \frac{2\pi}{[(1/K_{SAR}) - (1/K_{EMH})]} |\bar{K}|^{-4} \quad (19)$$

In this case the Doppler offset ω_D is identically zero.

We have chosen these particularly simple spectral approximations in order to clearly illustrate the fundamental physics of specular point scattering effects in the mean SAR image as well as to provide first numerical estimates these effects. Further investigations of specific imaging situations in which specular point scattering may play a role will clearly involve more sophisticated forms for the ocean wave spectrum. Because of complications introduced by the longwave field (as will be discussed in the next section), such investigations can best be carried out using Monte Carlo simulation of the SAR image [cf. *Alpers and Bruening*, 1986; C. Bruening et al., Monte Carlo simulation studies of the nonlinear imaging of a two dimensional surface wave field by a synthetic aperture radar, submitted to *International Journal of Remote Sensing*, 1987 (hereinafter referred to as Bruening et al., 1987)]. However, in this initial theoretical study, the additional complication introduced by such spectral forms would tend to obscure the fundamental physics, and our computations to date indicate that they do not add anything qualitatively new to the present discussion.

The sets of SAR parameters chosen correspond to the Seasat and SIR-B spaceborne SARs and to a typical airborne X band SAR. Together, these choices cover a range of typical SAR parameters. The parameters of the SIR-B SAR correspond to those used during orbit 106 on October 12, 1984, over the Chilean coast. This case is of special interest for this investigation, because a particularly small incidence angle was used ($\theta_i = 18°$).

According to Table 1, the computed coherence times range from approximately 10^{-1} s at L band (Seasat and SIR-B) to 3×10^{-2} s at X band. The directionality in the surface wave field causes an increase of approximately 20% in the coherence time relative to the isotropic cases. For the simple directionality function used here, τ_s is independent of the angle between the predominant wave propagation direction and SAR azimuth direction, Φ_o, while the Doppler offset varies sinusoidally with Φ_o. (We have also computed τ_s and ω_D using a $\cos^4(\Phi - \Phi_o/2)$ directionality and found in that case a very weak dependence of τ_s on Φ_o and a very weak modulation of the $\sin\Phi_o$ dependence of ω_D.)

Anticipating results needed in the next section relating the Doppler offset ω_D of a given scattering region to the resulting mean azimuthal displacement x_D in the SAR image, Table 1 also lists the mean azimuthal displacement

$$x_D = \frac{R_o}{2kV} \omega_D$$

Although the computed displacements will be somewhat modified by the local longwave slope (see section 4), it is apparent from the numbers shown in Table 1 that for SARs with high resolution or large ratios R_o/V, the image displacement relative to both the true ocean surface surface and the Bragg-scattering image (which displays no overall Doppler offset) can be appreciable for specular point imaging.

Finally, Table 1 shows the degradation ratio ρ_a'/ρ_a of the effective/nominal azimuthal resolution corresponding to the integration time/coherence time ratio T_i/τ_s (equation (26)). The coherence time is unaffected by the presence of a longwave field (see discussion in the next section). The actual azimuthal resolution is spatially modulated by the longwave orbital acceleration, but the ratio shown gives a good indication of the degradation in azimuthal resolution associated with specular point imaging.

4. Effects and Imaging of the Longwave Field

Our approach in this section is to reduce the reflectivity variance spectrum of the ocean surface in the presence of long waves to an expression involving the RVS derived in the last section in the absence of long waves. To do this, we first partition the ocean surface roughness spectrum yet again, as is shown in Figure 4. The second-partition wave number, K_{SAR}, is the wave number corresponding to the minimum wavelength surface component resolvable by the SAR. The resolution cutoff wave number is defined by the condition that either

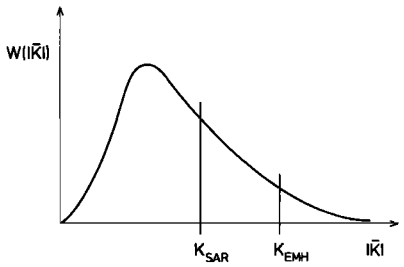

Fig. 4. Additional wave spectrum partition at K_{SAR} for SAR imaging theory.

the shorter wave components have wavelengths shorter than twice the nominal SAR resolution ρ_a or, alternatively, that shorter-wave components have periods shorter than the SAR integration time T_i [cf. *Hasselmann et al.*, 1985]. Hence

$$K_{SAR} = \frac{2\pi}{\lambda_{min}}$$

where

$$\lambda_{min} = \max\left\{2\rho_a, \frac{gT_i^2}{2\pi}\right\}$$

With this definition, we may now further divide large-scale spectral components (those for which $|\bar{K}| < K_{EMH}$) into "long-wave" ($|\bar{K}| < K_{SAR}$) and "intermediate-scale wave" ($K_{SAR} < |\bar{K}| < K_{EMH}$) components. The second-partition wave number K_{SAR} is typically at least an order of magnitude smaller than the first, K_{EMH}. For example, for the Seasat SAR, $K_{SAR} = 2\pi/50\text{ m} = 0.13\text{ m}^{-1}$ while $K_{EMH} = 2\pi/1.5\text{ m} = 4\text{ m}^{-1}$.

We model the effect of the longwave field on both scattering mechanisms simply as an overall tilt, advection, and acceleration of the nominal resolution cell, which we identify with the slope, orbital velocity and orbital acceleration of the long waves, respectively. In representing the longwave modulation of the specular point mechanism in this way, we choose not to use a coordinate system moving at the mean local specular point velocity. The motivation for such a coordinate translation is normally to capture most of the Doppler shift associated with the scattering mechanism within the coordinate transformation itself [cf. *Hasselmann et al.*, 1985]. While this technique is useful for Bragg scattering, it offers no significant simplification in the present application, since the residual Doppler broadening after removal of the mean Doppler shift by the coordinate transformation is still of the same order as the mean shift itself.

To proceed, let the reflectivity density of a given nominal resolution cell in a motionless longwave field be $\psi_o(x', y', t)$. In general, ψ_o depends on the longwave tilt, as well as on the geometrical and time variation properties of the intermediate-scale and small-scale waves, but not on the overall motion of the scattering region due to the longwave field. The overall motion gives rise to additional phase variations in the signal scattered back to the SAR from this region which affect the output of the SAR processor. *Raney* [1971] has derived an approximation for this phase variation by expanding the target range variation as a function time about the instant when the target is directly abeam of the SAR, t'. Keeping only the first two terms in the series expansion, Raney finds an expression for the phase variation involving target velocity and acceleration. His expression has been applied to the case of a scattering region on the ocean surface by *Alpers and Rufenach* [1979]. The phase variation may be expressed, to a good approximation, as

$$\Delta(x', y', t) = -2ikV_R(x', y')(t - t') - kA_R(x', y')(t - t')^2 \quad (20)$$

where V_R and A_R are the longwave velocity and acceleration in the SAR range direction, averaged over the integration time and centered at t' [*Alpers and Rufenach*, 1979; *Hasselmann et al.*, 1985]. The approximation is justified provided that the shortest longwave spectral components have periods much longer than the SAR integration time, as has already been stipulated.

Following the derivation of equation (A1) [cf. *Harger*, 1970; *Alpers and Rufenach*, 1979; *Hasselmann et al.*, 1985], the full reflectivity density including overall motion effects is then given by

$$\psi(x', y', t) = \psi_o(x', y', t) \cdot \exp\left[-2ikV_R(x', y')(t-t') - ikA_R(x', y')(t-t')^2\right] \quad (21)$$

From this and equations (4) and (6) we obtain for the reflectivity variance spectrum, after some manipulation,

$$\Psi(x', y', T_i, \omega) = V^2[2(T_i^{-2} + T_s^{-2})]^{-1} \cdot \exp\left[-4(T_i^{-2} + T_s^{-2})\left(\frac{R_o\omega}{2kV^2}\right)^2\right] \int dt_D \Psi_o(x', y', T_i, t_D) \cdot \exp\left\{-t_D^2\left[T_i^{-2} + T_s^{-2} + \frac{k^2A_R^2(x', y')}{\pi(T_i^{-2} + T_s^{-2})}\right]\right\} \cdot \exp\left\{-i\left[\left(1 - \frac{R_oA_R(x', y')}{V^2(1 + T_s^2/T_i^2)}\right)\omega - 2kV_R(x', y')\right]t\right\} \quad (22)$$

where $t_C = \frac{1}{2}(t_2 + t_1)$ and $t_D = t_2 - t_1$, and where we have defined

$$\Psi_o(x', y', t_i, t_D) = \frac{1}{\sigma(x', y')}\langle\psi_o(x', y', t_1)\psi_o^*(x', y', t_2)\rangle \quad (23)$$

We have assumed that Ψ_o is a slowly varying function of t_C and thus may be approximated by its average value in this variable over the SAR integration time. This, together with the dependence of V_R and A_R on T_i, accounts for the dependence of Ψ_o on the integration time.

The only longwave effect left to consider is tilt. To describe this effect, begin by considering the situation shown in Figure 5. The illuminating radiation from the SAR is considered plane over the scattering region and incident from the direction defined by θ_i, ϕ_i. According to Figure 1, $\phi_i = -\pi/2$, but again it is useful for the moment to leave ϕ_i unspecified. The normal of the mean surface is no longer vertical but points in the direction defined by the polar angle θ' and azimuthal angle ϕ'. This corresponds to tilting by a longwave field having local slopes $\partial h_M/\partial x = \tan\theta'\cos\phi'$ and $\partial h_M/\partial y = \tan\theta'\sin\phi'$ in the x and y directions, respectively.

In order to compute the backscatter cross section in the presence of tilt, one normally considers a local coordinate system with one axis along the local longwave field normal and decomposes the incident radiation into components which are horizontally and vertically polarized in this local coordinate system. The scattered field is computed in the local coordinate system and then transformed back to the original coordinates in order to compute the scattering cross section [cf. *Valenzuela*, 1968]. However, in cases where physical optics applies, the magnitude of the scattered field is (approximately) independent of polarization [*Stogryn*, 1967], and thus the po-

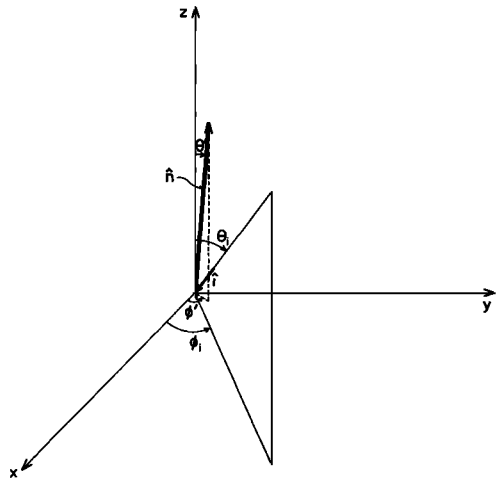

Fig. 5. Scattering from a tilted surface region. The local unit surface normal is $\hat{n}$, which is characterized by angles θ' and ϕ'.

larization decomposition is unnecessary. It is shown in Appendix C that the physical optics backscatter cross section of a surface region with small overall mean slopes $\partial h_M/\partial x$ and $\partial h_M/\partial y$ may be written approximately in the form of (12) with (13)–(15) unchanged except for the replacement of $\bar{K}_i$ by an effective $\bar{K}_i'$ given by

$$K_{ix}' = K_{ix} - k_z(\bar{K}_i)\frac{\partial h_M}{\partial x}$$
$$K_{iy}' = K_{iy} - k_z(\bar{K}_i)\frac{\partial h_M}{\partial y} \tag{24}$$

The quantity $k_z(\bar{K}_i)$ remains unchanged. From (13)–(15), we see that in general, the quantities σ and ω_D may be modified locally by the longwave tilt.

Writing $\Psi_o(x', y', T_i, t_D)$ in order to explicitly display the possible variation of ω_D with position in the longwave field, and using (21)–(23) in (5) and (6), we arrive at the following somewhat simpler equation for the mean SAR intensity image:

$$\langle I(x, y)\rangle = \frac{(VT_i)^2}{2}\left(\frac{\pi}{1 + T_i^2/T_s^2}\right)^{1/2} \cdot \int dx' \int dy' \sigma(x', y') |T_R(y - y', y, h)|^2 \frac{\rho_a}{\rho_a'(x', y')} \cdot \exp\left\{\frac{-\pi^2}{\rho_a'^2(x', y')}\left[\left(1 - \frac{R_o A_R}{V^2(1 + T_s^2/T_i^2)}\right)(x - x') - x_D - \frac{R_o}{V} V_R\right]\right\} \tag{25}$$

where the effective SAR azimuthal resolution ρ_a' is given by

$$\rho_a' = \rho_a\left(1 + \frac{T_i^2}{T_s^2} + \frac{T_i^2}{\tau_s^2} + \frac{k^2 A_R^2(x', y')T_i^4}{4(1 + T_i^2/T_s^2)}\right)^{1/2}$$
$$\rho_a = \frac{\pi R_o}{kVT_i} \tag{26}$$

and where the standard relation between Doppler offset frequency and azimuthal image displacement has been used.

$$x_D = \frac{R_o}{2kV}\omega_D \tag{27}$$

Notice that a short coherence time (i.e., a broad Doppler spectrum) causes a reduction in the total image intensity through the factor ρ_a/ρ_a'. This is a manifestation of the reduction of image intensity associated with wide bandwidth scattering mechanisms mentioned earlier.

It can readily be shown that the term $1 - [R_o A_R/V^2(1 + T_s^2/T_i^2)]$ differs from 1 by less than 1% for typical SAR parameters and ocean wave orbital acceleration. Thus this term may be neglected, leaving us with

$$\langle I(x, y)\rangle = \frac{(VT_i)^2}{2}\left(\frac{\pi}{1 + T_i^2/T_s^2}\right)^{1/2} \cdot \int dx' \int dy' \sigma(x', y') |T_R(y - y', y, h)|^2 \frac{\rho_a}{\rho_a'(x', y')} \cdot \exp\left\{\frac{-\pi^2}{\rho_a'^2(x', y')}\left[x - x' - x_D - \frac{R_o}{V} V_R\right]\right\} \tag{28}$$

which is an equation identical in form to that used by *Alpers and Bruening* [1986] in their simulation of SAR ocean wave imaging for the case when Bragg scattering is the dominant scattering mechanism. In their case, however, the physical meaning and numerical values of τ_s are different, and $x_D = \omega_D = 0$.

To complete our investigation, we need to examine the variation of σ and ω_D with local longwave slope. Consider first the Doppler offset ω_D. Rewrite (15) for ω_D, specializing to the geometry of Figure 1 ($\phi_i = -\pi/2$, $K_{ix} = 0$), and using the effective $\bar{K}_i'$ in place of $\bar{K}_i$,

$$\omega_D = \left(1 - \frac{C_{xy}^2}{4|C_{xx}||C_{yy}|}\right)^{-1} K_{iy}'\left(\frac{C_{yt}}{|C_{yy}|} + \frac{C_{xt}C_{xy}}{2|C_{xx}||C_{yy}|}\right).$$

Using (7c) and (24),

$$\omega_D = k \sin\theta_i\left[1 - \frac{\partial h_M/\partial y}{\tan\theta_i}\right]\left(1 - \frac{C_{xy}^2}{4|C_{xx}||C_{yy}|}\right)^{-1} \cdot \left(\frac{C_{yt}}{|C_{yy}|} + \frac{C_{xt}C_{xy}}{2|C_{xx}||C_{yy}|}\right) \tag{29}$$

At an incidence angle of 18°, longwave slopes of 5° in the range direction cause a variation in $1 - (\tan\theta_i)^{-1}\,\partial h_M/\partial y$ of roughly 25%. This can cause the azimuthal displacement of a given resolution cell (scattering region) to vary by the same percentage along a longwave profile (compare equations (27)–(29)). However, as is shown next, usually only particular resolution cells on the longwave profile actually contribute to the SAR image.

By far the strongest tilt modulation appears in the variation of σ. Using (24) in (13) and neglecting terms of second order and higher in the longwave slopes, we obtain

$$\sigma(x', y') = \sigma_o(x', y')M\left(x', y', \frac{\partial h_M}{\partial x}, \frac{\partial h_M}{\partial y}\right) \tag{30}$$

where $\sigma_o(x', y')$ is the unmodified frozen surface backscatter cross section in the absence of tilt, given by (13), and where the tilt modulation factor M is given by

$$M\left(x', y', \frac{\partial h_M}{\partial x}, \frac{\partial h_M}{\partial y}\right) = \exp\left\{-\tan\theta_i\left(1 - \frac{C_{xy}^2}{4|C_{xx}||C_{yy}|}\right)\right. \cdot \cos\phi_i \frac{\partial h_M}{\partial x}\left[(\overline{h_I^2}|C_{xx}|)^{-1} + \frac{C_{xy}}{|C_{xx}||C_{yy}|}\right] + \left.\sin\phi_i \frac{\partial h_M}{\partial y}\left[(\overline{h_I^2}|C_{yy}|)^{-1} + \frac{C_{xy}}{|C_{xx}||C_{yy}|}\right]\right\} \tag{31}$$

Except at very small incidence angles θ_i and/or for extremely small longwave slopes, the variation of M with longwave slope is very strong and normally cannot be approximated by a tilt modulation transfer function which is linear in the longwave slopes. Physically, this is because the number of surface points within a typical scattering region which have slopes sufficiently large to produce a local specular return decreases very rapidly with increasing incidence angle in the range $\theta_i > 15°$. Longwave tilt of the scattering region toward the SAR strongly modulates the number of backscattering specular points and thus strongly modulates the backscatter cross section. This modulation appears to be considerably stronger than typical hydrodynamic modulation factors for intermediate-scale waves propagating in a longwave field, and so we will not consider the latter in the following.

The effect of this strong tilt modulation on the mean SAR image is to cause those parts of the scene with longwave tilt toward the SAR to be strongly brightened, even when the specular point return from the rest of the scene remains comparatively small. As an example, we have computed σ_o and M near $\theta_i = 18°$ in decibels for the case of the SIR-B SAR and the Phillips spectrum with $\cos^2$ directionality used in section 3. At $\theta_i = 18°$, σ_o is -48.2 dB, which is small in comparison with the Bragg scattering cross-section of approximately -20 dB at this incidence angle. However, the slope modulation M in this case (setting $\phi_i = -(\pi/2)$ in (31) and transforming to decibels) is given by

$$10 \log_{10} M = 4.343 \left\{ \left[\frac{\partial h_M}{\partial y} \tan \theta_i \left(1 - \frac{C_{xy}^2}{4 |C_{xx}||C_{yy}|} \right)^{-1} \right] \cdot \left[\overline{(h_I^2 |C_{yy}|)^{-1}} + \frac{C_{xy}}{|C_{xx}||C_{yy}|} \right] \right\} \text{ dB} = 436.9 \frac{\partial h_M}{\partial y} \text{ dB} \quad (32)$$

Thus, a 5° longwave slope toward the SAR produces a local backscatter cross section of roughly -10 dB. Range-traveling waves are evidently most likely to produce such a modulation and contribute to the specular point SAR image. The short specular point coherence time and consequent low azimuthal resolution will (in the mean) cause this strongly modulated contribution to be smeared out in the azimuth direction in the specular point image. Since range resolution is unaffected by specular point scattering, there should be no smearing in range. The brightness of the specular point contribution will be reduced in most cases because its Doppler bandwidth exceeds the SAR system bandwidth.

Even for individual realizations of SAR intensity images, tilt modulation and smearing would occur because of the behavior of individual specular points [*Longuet-Higgins*, 1960*a*, *b*, *c*], leading to azimuthally oriented streaks superimposed on the Bragg-scattering ocean surface image. As noted in the introduction, an example of azimuthal streaks in a Seasat image of a high-wind area is presented by *Jenkins et al.* [1984]. The apparent length of the streaks in this image varies between approximately 100 and 500 m, with an average length of approximately 300 m. From Table 1, we would expect a specular point contribution from a given resolution cell to be spread in the image azimuthally over 6 to 7 times the nominal SAR resolution for the Seasat SAR, because of the 0.09-s specular point scattering coherence time in this case. Given the nominal Seasat azimuthal resolution of 25 m, this gives a rough estimate for the expected streak length of 250 to 275 m, which agrees well the observed streak lengths. A second image of a region approximately 600 km away on the same Seasat orbit shows little or no streaking; thus the streaking appears not to be a system artifact. Azimuthal streaks have also been reported by *Shuchman et al.* [1983] and *Lyzenga et al.* [1985], but because of the large incidence angles in these studies, these streaks appear to have been caused by some scattering mechanism other than specular point scattering. Nonetheless, the effects of specular point scattering streaks on the image spectrum can be expected to be similar to those observed by these authors, namely, the introduction of noise along the SAR azimuth wave number axis. Depending on the width of the surface wave spectrum, harmonics of the dominant ocean wavelength may also appear because of the strong, nonlinear tilt modulation of specular point scattering. However, as is discussed below, this topic requires further investigation. Data from the Tower Ocean Wave and Radar Dependence (TOWARD) experiment [*Shemdin et al.*, 1986] should in the future prove very useful for further testing of image models which include specular point scattering, since these data extends to small incidence angles.

The tilt modulation effects just discussed, together with equations (28)–(31), provide a general description of the mean SAR specular point scattering intensity image and lay the theoretical groundwork for future work. Further theoretical investigation should consider the effects of specular point scattering on the total (Bragg scattering and specular point scattering) SAR image spectrum, interactions between specular point scattering effects, and should make use of more sophisticated approximations for the ocean wave spectrum. This can in principle be accomplished using the same nonlinear Monte Carlo simulation techniques used by *Alpers and Bruening* [1986] and *Bruening et al.* [1987] and would lead to quantification of the conditions under which specular point scattering effects are significant as well as better quantification of the effects themselves. This will enable a detailed comparison of the SAR imaging model including specular point effects with data.

5. Discussion and Conclusions

We have combined the composite roughness theory of electromagnetic wave scattering from the ocean surface with the SAR ocean wave imaging theory of *Hasselmann et al.* [1985] to investigate the specular point scattering contribution the mean SAR intensity image.

Specular points on the ocean surface move with considerable speed on nonuniform paths and tend to be short-lived, giving rise to wide bandwidth, strongly Doppler-shifted return signals. This causes imaged individual scattering regions in the mean SAR image to be significantly displaced and smeared azimuthally relative to both the true scene and the SAR Bragg-scattering image. The mean displacements and smearing are generally of the same order and can vary, depending on ocean wave and SAR parameters, from some tens of meters to a few hundred meters. The wide bandwidth of the specular scatterers will often exceed the SAR system bandwidth, resulting in a loss of the overall mean specular point image intensity.

For most ocean wave conditions and SAR incidence angles greater than 15°, the specular point scattering contribution to the mean image intensity is small, even without bandwidth losses, compared with the Bragg-scattering contribution. However, their contribution to the actual ocean wave image,

i.e., to the wave image contrast, can become significant. In general, the long wave modulation of specular scatterers is dominated by the tilt modulation and is strongly nonlinear. For waves of 5° slope at a SAR incidence angle of 18°, for example, our numerical estimates yield a strongly nonlinear local modulation of the specular point cross section about a mean of −48 dB with a maximum cross section of −10 dB for wave slopes maximally tilted toward the SAR. This should be compared with a mean Bragg cross section at this incidence angle of the order of −20 dB with a typical modulation depth of the order of 3 dB. The combination of specular point effects discussed here can lead to azimuthal streaking which is qualitatively consistent with observed azimuthal streaking at small incidence angles.

The present paper lays the theoretical groundwork for further analysis of the contribution of the specular point return to SAR imaging and thus should be regarded only as a first step. Our computations of specular point return imaging properties were based on two rather simple wave spectrum models, namely, a Phillips frequency spectrum with a sharp low-wave number cutoff and either a $\cos^2\theta$ or an isotropic directional distribution. More extensive computations of these relations for a wider variety of ocean wave spectra would be useful.

Although the theoretical analysis of the longwave modulation of the specular return was carried out for the general case of an arbitrary longwave field, detailed numerical computations of the nonlinear mapping between the surface wave field and the combined specular and Bragg scattering SAR image for an arbitrary two-dimensional wave spectrum also lie beyond the scope of the present paper. However, such computations can in principle be carried out using the same nonlinear Monte Carlo simulation techniques as was applied by *Alpers and Bruening* [1986] and Bruening et al. (1987) to the Bragg scattering image of of surface waves. Finally, we have considered neither the effects of SAR processor focus adjustments nor the speckle statistics of the specular point image. Studies of these topics would similarly represent useful extensions of the present study.

Although further investigation may prove otherwise, it appears on the basis of our present results that situations involving significant specular point scattering are best avoided when remote sensing of the ocean surface wave spectrum is the objective, because of the short coherence time and nonlinear spatial modulation associated with this scattering mechanism. Avoidance of specular point scattering typically means operation at larger incidence angles. However, such operation has other disadvantages. Thus it is necessary to further quantify the conditions (e.g., incidence angle, wind, and current conditions) under which specular point scattering significantly contributes to the backscattered signal and to further quantify imaging conditions under which the SAR image spectrum is affected by this mechanism. These goals will also be advanced by the further studies listed above.

APPENDIX A

Consider a SAR system of the type described at the beginning of section 2. The slant range R_o of a particular point on the surface is determined by the ground range y of the surface point and platform altitude h. The platform position x is related to an equivalent time variable t via the equation $t = x/V$, where V is the speed of the platform. The received signal at platform position x and apparent ground range y may then be modeled as follows [cf. *Harger*, 1970; *Raney*, 1980; *Hasselmann et al.*, 1985]:

$$c_1(x_1, y) = \int dx_2 D(x_1 - x_2, y, h) H_1(x_1 - x_2, y, h) \cdot \int dy_2 T_R(y - y_2, h) \psi\left(x_2, y_2, \frac{x_1}{V}\right) \quad \text{(A1)}$$

where ψ is the reflectivity density of the surface, D is the linear Doppler frequency modulation factor

$$D(x_1 - x_2, y, h) = \exp\left[\frac{ik}{R_o(y, h)}(x_1 - x_2)^2\right] \quad \text{(A2)}$$

H_1 is a function essentially determined by the two-way real aperture illumination pattern on the mean surface $A_H(x_1 - x_2, y, h)$ via the equation

$$H_1(x_1 - x_2, y, h) = \frac{\exp[2ikR_o(y, h)]}{R_o^2(y, h)} A_H(x_1 - x_2, y, h) \quad \text{(A3)}$$

and where $T_R(y - y_2, y, h)$ is the SAR impulse response in the y coordinate. T_R may include both pulse width and illumination pattern effects, and thus it depends on both y and h. In most applications, T_R is a very narrow function of $y - y_2$.

In general, the weak variation of A_H and $1/R_o$ with slant range R_o must be taken into account when processing SAR data. It is not difficult, however, to generalize results obtained by neglecting this variation. Thus we will treat R_o as constant in this theoretical development while remembering the practical importance of its variation. In this study we model A_H as a Gaussian function, and thus H_1 is given by

$$H_1(x_1 - x_2, y, h) = \frac{\exp[2ikR_o]}{R_o^2} \exp\left[-\frac{2(x_1 - x_2)^2}{(VT_i)^2}\right] \quad \text{(A4)}$$

where T_i is the SAR integration time. This particular definition is chosen for consistency with the work of *Alpers and Bruening* [1986], *Alpers et al.* [1986], and earlier work.

The complex image of the surface is usually obtained by applying a matched filter in order to "dechirp" or focus the frequency modulated received signal,

$$c_2(x, y) = \int dx_1 \int dx_2 D(x_1 - x_2, y, h) D^*(x - x_1, y, h) \cdot H_1(x_1 - x_2, y, h) H_2(x - x_1, y, h) \cdot \int dy_2 T_R(y - y_2, y, h) \psi\left(x_2, y_2, \frac{x_1}{V}\right) \quad \text{(A5)}$$

where

$$H_2(x - x_1, y, h) = \exp[2ikR_o] \exp\left[-\frac{2(x - x_1)^2}{(VT_s)^2}\right] \quad \text{(A6)}$$

Note that the quantity T_s in the SAR processing filter need not be equal to the SAR integration time T_i. Making the change of variable $x' = x_1 - x_2$ and defining

$$\omega = \frac{2kV}{R_o}(x - x_2) \quad \text{(A7)}$$

(A5) may be written

$$c_2(x, y) = \int dx_2 \int dy_2 \exp\left[-\frac{ik}{R_o}(x - x_2)^2\right] \cdot T_R(y - y_2, y, h) \tilde{\psi}(x_2, y_2, \omega) \quad \text{(A8)}$$

where

$$\tilde{\psi}(x_2, y_2, \omega) = V \int dt' H_1(Vt') H_2\left(\frac{R_o\omega}{2kV} - Vt'\right) \cdot \psi(x_2, y_2, t_2 + t') \exp[i\omega t'] \quad \text{(A9)}$$

$$t_2 = \frac{x_2}{V} \qquad t' = \frac{x'}{V}$$

Next, we form the mean SAR intensity image $\langle |c_2(x, y)|^2 \rangle$. Using the spatial whiteness assumption

$$\langle \psi(x_2, y_2, t)\psi^*(x_2', y_2', t') \rangle = \sigma(x_2, y_2)\Psi(x_2, y_2, t, t')\delta(x_2 - x_2')\delta(y_2 - y_2') \quad \text{(A10)}$$

we obtain

$$\langle I(x, y) \rangle = \langle |c_2(x, y)|^2 \rangle = \int dx_2 \int dy_2 \sigma(x_2, y_2) |T_R(y - y_2)|^2 \cdot \Psi\left[x_2, y_2, T_i, T_s, \frac{2kV}{R_o}(x - x_2)\right] \quad \text{(A11)}$$

where

$$\Psi(x_2, y_2, T_i, T_s, \omega) = V^2 \int dt_1' \int dt_2' \varepsilon^{-i\omega(t_2 - t_1)} \cdot H(t_1', \omega) H^*(t_2', \omega) \Psi(x_2, y_2, t_1', t_2') \quad \text{(A12)}$$

$$H(t', \omega) = H_1(VT') H_2\left(\frac{R_o\omega}{2kV} - Vt'\right) \quad \text{(A13)}$$

Finally, the expression for Ψ may be somewhat simplified using the definitions of H_1 and H_2. Defining sum and difference coordinates

$$t_C = \tfrac{1}{2}(t_2' + t_1') \qquad t_D = t_2' - t_1'$$

and ignoring the factor $1/R_o^2$ in H_1, we find that

$$\Psi(x_2, y_2, T_i, T_s, \omega) = V^2 \int dt_C \int dt_D \exp[-i\omega t_D] \Psi(x_2, y_2, t_C, t_D) \cdot \exp\left\{-4\left[\frac{t_C^2}{T_i^2} + \frac{(t_C - R_o\omega/2kV)^2}{T_s^2}\right] - t_D^2\left(\frac{1}{T_i^2} + \frac{1}{T_s^2}\right)\right\} \quad \text{(A14)}$$

which is precisely equation (6) in section 2.

APPENDIX B

Consider the physical optics time-correlated cross section given by equation (9). Expand $h_L(\bar{R}_2, t_2)$ in a Taylor series about $\bar{R}_1, t_1$,

$$h_L(\bar{R}_2, t_2) \approx h_L(R_1, t_1) + t_D \left.\frac{\partial h_L}{\partial t}\right|_{\bar{R}_1, t_1} + x_D \left.\frac{\partial h_L}{\partial x}\right|_{\bar{R}_1, t_1} + y_D \left.\frac{\partial h_L}{\partial y}\right|_{\bar{R}_1, t_1} + t_D^2 \left.\frac{\partial^2 h_L}{\partial t^2}\right|_{\bar{R}_1, t_1} + x_D^2 \left.\frac{\partial^2 h_L}{\partial x^2}\right|_{\bar{R}_1, t_1} + y_D^2 \left.\frac{\partial^2 h_L}{\partial y^2}\right|_{\bar{R}_1, t_1} + x_D t_D \left.\frac{\partial^2 h_L}{\partial x\, \partial t}\right|_{\bar{R}_1, t_1} + y_D t_D \left.\frac{\partial^2 h_L}{\partial y\, \partial t}\right|_{\bar{R}_1, t_1} + x_D y_D \left.\frac{\partial^2 h_L}{\partial x\, \partial y}\right|_{\bar{R}_1, t_1} + \cdots \quad \text{(B1)}$$

where

$$x_D = x_2 - x_1 \qquad y_D = y_2 - y_1 \qquad t_D = t_2 - t_1 \quad \text{(B2)}$$

Further, let us define $\bar{\kappa}_i$ and $\beta(\bar{\kappa}_i)$ by

$$k\bar{\kappa}_i = \bar{K}_i \qquad k\beta(\bar{\kappa}_i) = k_z(\bar{K}_i) \quad \text{(B3)}$$

Evidently (compare equation (7c), section 3),

$$\kappa_{ix} = \sin\theta_i \cos\phi_i \qquad \kappa_{iy} = \sin\theta_i \sin\phi_i \qquad \beta(\bar{\kappa}_i) = \cos\theta_i$$

Substituting (B1)–(B3) into (9), we obtain

$$\sigma_t(x', y', t_1, t_2) = \frac{k^2 |F(0)|^2}{\cos^2\theta_i} \iint dx_D\, dy_D \exp[2ik(\kappa_{ix}x_D + \kappa_{iy}y_D)] \cdot \left\langle \exp\left\{2ik\beta(\bar{\kappa}_i)\left[t_D \left.\frac{\partial h_L}{\partial t}\right|_{\bar{R}_1, t_1} + x_D \left.\frac{\partial h_L}{\partial x}\right|_{\bar{R}_1, t_1} + y_D \left.\frac{\partial h_L}{\partial y}\right|_{\bar{R}_1, t_1} + t_D^2 \left.\frac{\partial^2 h_L}{\partial t^2}\right|_{\bar{R}_1, t_1} + x_D^2 \left.\frac{\partial^2 h_L}{\partial x^2}\right|_{\bar{R}_1, t_1} + y_D^2 \left.\frac{\partial^2 h_L}{\partial y^2}\right|_{\bar{R}_1, t_1} + x_D t_D \left.\frac{\partial^2 h_L}{\partial x\, \partial t}\right|_{\bar{R}_1, t_1} + y_D t_D \left.\frac{\partial^2 h_L}{\partial y\, \partial t}\right|_{\bar{R}_1, t_1} + x_D y_D \left.\frac{\partial^2 h_L}{\partial x\, \partial y}\right|_{\bar{R}_1, t_1} + \cdots\right]\right\}\right\rangle \quad \text{(B4)}$$

Provided that the surface roughness statistics are stationary, the expectation value in (B4) depends temporally only on the lag, $t_D = t_2 - t_1$. By virtue of the problem formulation used in this paper (compare section 2 and *Ishimaru* [1978]), the Fourier transform of σ_t with respect to t_D yields the spectrum of the backscattered signal frequency variation about the carrier frequency ω_D. This is just the Doppler spectrum which arises from the motion of the scattering surface. Thus we are motivated to consider

$$\sigma_\omega(\omega) = \int dt_D \exp[-i\omega t_D]\sigma_t(t_D) \quad \text{(B5)}$$

Because we are interested in σ_ω at large wave numbers k, we make the following change of variables:

$$x'' = 2k\beta(\bar{\kappa}_i)x_D \quad \text{(B6a)}$$

$$y'' = 2k\beta(\bar{\kappa}_i)y_D \quad \text{(B6b)}$$

$$t'' = 2k\beta(\bar{\kappa}_i)t_D \quad \text{(B6c)}$$

Then using (B4)–(B6), we obtain

$$\sigma_\omega(\omega) = \frac{|F(0)|^2}{8k\cos^5\theta_i} \int dt'' \int dx'' \int dy'' \cdot \exp\left[i\frac{\kappa_{ix}}{\beta(\bar{\kappa}_i)}x'' + i\frac{\kappa_{iy}}{\beta(\bar{\kappa}_i)}y'' - i\left(\frac{\omega}{2k\beta(\bar{\kappa}_i)}\right)t''\right] \cdot \left\langle \exp\left\{ix'' \left.\frac{\partial h_L}{\partial x}\right|_{\bar{R}_1, t_1} + iy'' \left.\frac{\partial h_L}{\partial y}\right|_{\bar{R}_1, t_1} + it'' \left.\frac{\partial h_L}{\partial t}\right|_{\bar{R}_1, t_1} + O\left(\frac{1}{k}\right)\right\}\right\rangle \quad \text{(B7)}$$

In the case where k is large (although still finite), we may neglect terms of order 1 and higher in inverse powers of k in the exponential argument of the expectation in (B7). Within this approximation, the right-hand side of this equation is a characteristic function, from which we obtain

$$\sigma_\omega(\omega) \approx \frac{\pi^3 |F(0)|^2}{k\cos^5\theta_i} \cdot P_{(\partial h_L/\partial x),(\partial h_L/\partial y),(\partial h_L/\partial t)}\left(\frac{\kappa_{ix}}{\beta(\bar{\kappa}_i)}, \frac{\kappa_{iy}}{\beta(\bar{\kappa}_i)}, -\frac{\omega}{2k\beta(\bar{\kappa}_i)}\right) \quad \text{(B8)}$$

where we have used the relation between a trivariate PDF and its characteristic function

$$P_{x,y,z}(x', y', z') = \frac{1}{(2\pi)^3} \iiint dx'' \, dy'' \, dz''$$

$$\cdot \exp [ix'x'' + iy'y'' + iz'z''] \langle \exp [ix''x + iy''y + iz''z] \rangle$$

The Doppler spectrum at frequency ω is simply proportional to the joint PDF of the surface slopes and the time derivative of surface height at a point, evaluated at the specular reflection values for backscatter

$$\frac{\kappa_{ix}}{\beta(\bar{\kappa}_i)} = \tan \theta_i \cos \phi_i \qquad \frac{\kappa_{iy}}{\beta(\bar{\kappa}_i)} = \tan \theta_i \sin \phi_i$$

and at the value of $\partial h_L/\partial t$ which causes reflection from the specular point to be Doppler shifted by an amount ω from the carrier frequency.

The latter point can be clearly seen by inspection of Figure B1. The surface point with proper local slope for specular reflection has an instantaneous vertical velocity of $\partial h_L/\partial t$ and thus has an instantaneous velocity component $\partial h_L/\partial t \cos \theta_i$ along the radar line of sight. This gives rise to the Doppler shift $\omega = 2k \, \partial h_L/\partial t \cos \theta_i$ in the signal scattered from the surface near this point.

In conclusion, note that this derivation is essentially a straightforward generalization of the work of *Barrick* [1968*b*], with one small difference. Barrick considered the scattering cross section of a stationary surface in the limit as $k \to \infty$. In the present case, k is taken to be large but still finite, in order that the term Doppler spectrum of the scattered signal remain defined.

APPENDIX C

Consider the integral expression for the physical optics cross section given by (9).

$$\sigma_t^{po}(x', y', t_1, t_2) = \frac{k^2 |F(0)|^2}{\cos^2 \theta_i} \int d^2R_D \exp [2i\bar{K}_i \cdot \bar{R}_D]$$

$$\cdot \langle \exp \{-2ik_z(\bar{K}_i)[h_L(\bar{R}_2, t_2) - h_L(\bar{R}_1, t_1)]\} \rangle \qquad \text{(C1)}$$

$$\bar{R}_D = \bar{R}_2 - \bar{R}_1$$

It is known that in the high-frequency limit, the main contribution to this integral comes from the region around $|\bar{R}_D| = 0$. Thus to consider the case in which $h_L(R, t)$, the large-scale rough surface height, has an overall mean slope, we write h_L as follows:

$$h_L(\bar{R}_1, t_1) = h_M - \tfrac{1}{2}\nabla h_M \bar{R}_D + \tilde{h}(\bar{R}_1, t_1) \qquad \text{(C2a)}$$

$$h_L(\bar{R}_2, t_2) = h_M + \tfrac{1}{2}\nabla h_M \bar{R}_D + \tilde{h}(\bar{R}_2, t_2) \qquad \text{(C2b)}$$

where h_M is the height of the mean, tilted surface and where $\tilde{h}$ is the variation in the $\hat{z}$ direction of the rough surface height not accounted for by the overall surface slope. Thus

$$h_L(\bar{R}_2, t_2) - h_L(\bar{R}_1, t_1) = \nabla h_M \bar{R}_D + [\tilde{h}(R_2, t_2) - \tilde{h}(\bar{R}_1, t_1)] \qquad \text{(C3)}$$

Since the longwave slopes are considered deterministically for a given realization of the longwave field, we take the exponential factors involving these slopes outside the expectation and obtain

$$\sigma_t^{po}(x', y', t_1, t_2) = \frac{k^2 |F(0)|^2}{\cos^2 \theta_i} \int d^2R_D \exp [2i\bar{K}_i' \cdot \bar{R}_D]$$

$$\cdot \langle \exp \{-2ik_z(\bar{K}_i)[\tilde{h}(\bar{R}_2, t_2) - \tilde{h}(\bar{R}_1, t_1)]\} \rangle \qquad \text{(C4)}$$

where

$$K_{ix}' = \bar{K}_i' \hat{x} = K_{ix} - k_z(\bar{K}_i) \frac{\partial h_M}{\partial x} \qquad \text{(C5a)}$$

and

$$K_{iy}' = \bar{K}_i' \hat{y} = K_{iy} - k_z(\bar{K}_i) \frac{\partial h_M}{\partial y} \qquad \text{(C5b)}$$

This expression is simply the original formula for the physical optics time-correlated backscatter cross section, but evaluated at modified values of K_{ix} and K_{iy} given by K_{ix}' and K_{iy}', with one small difference. In the original cross section deviation, h_L was taken to be the rough surface height variation normal to the mean (planar, untilted) surface. In equation C4, $\tilde{h}$ is the additional rough surface height variation in the $\hat{z}$ direction, which is not normal to the mean tilted surface. However, the difference between the correlation functions of the two displacements (which is what appears when the expectations are carried out assuming a Gaussian distribution of displacements in each case) is of second order in the mean surface slopes $\partial h_L/\partial x$ and $\partial h_L/\partial y$ and thus may be neglected provided that these slopes are small.

Thus we obtain the result cited in section 4.

Acknowledgments. We thank Claus Bruening and Jens Schroeter for helpful discussions. This work was sponsored by the Office of Naval Research.

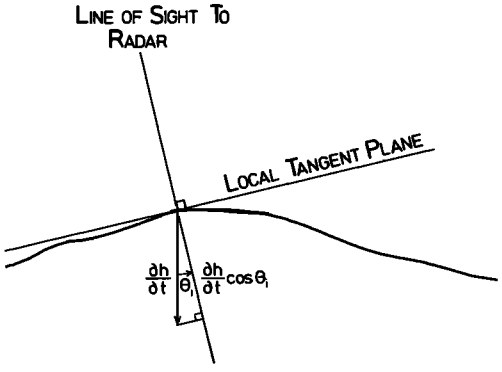

Fig. B1. Instantaneous specular point motion (θ_i is the radar angle of incidence, and h is the rough surface height at the specular point).

REFERENCES

Alpers, W. R., and C. Bruening, On the relative importance of motion-related contributions of the SAR imaging mechanism of ocean surface waves, *IEEE Trans. Geosci. Remote Sens.*, *GE-24*(6), 873–885, 1986.

Alpers, W. R., and K. Hasselmann, The two-frequency microwave technique for measuring ocean-wave spectra from an airplane or satellite, *Boundary Layer Meteorol.*, *13*, 215–230, 1978.

Alpers, W. R., and C. L. Rufenach, The effect of orbital motions on synthetic aperture radar imagery of ocean waves, *IEEE Trans. Antennas Propag.*, *AP-27*(5), 685–690, 1979.

Alpers, W. R., D. B. Ross, and C. L. Rufenach, On the detectability of ocean surface waves by real and synthetic aperture radar, *J. Geophys. Res.*, *86*(C7), 6481–6498, 1979.

Alpers, W. R., C. Bruening, and K. Richter, Comparison of simulated and measured synthetic aperture radar image spectra with buoy-derived ocean wave spectra during the Shuttle Imaging Radar–B mission, *IEEE Trans. Geosci. Remote Sens.*, *GE-24*(4), 559–566, 1986.

Barrick, D. E., Rough surface scattering based on the specular point theory, *IEEE Trans. Antennas Propag., AP-16*(4), 449–454, 1968*a*.

Barrick, D. E., Relationship between slope probability density function and the physical optics integral in rough surface scattering, *Proc. IEEE, 56*(10), 1728–1729, 1968*b*.

Bass, F. G., I. M. Fuks, A. I. Kalinowsky, I. E. Ostrowsky, and A. D. Rosenberg, Very high frequency radio wave scattering by a disturbed sea surface, *IEEE Trans. Antennas Propag., AP-16*(5), 560–568, 1968.

Brown, G. S., Backscattering from a Gaussian-distributed, perfectly conducting rough surface, *IEEE Trans. Antennas Propag., AP-26*, 472–482, 1978.

Brown, G. S., A study of terrain scattering physics, *Rep. RADC-TR-89-369*, Rome Air Development Center, Feb. 1981. (Available from the Defense Technical Information Center, Alexandria, Va.).

Cooper, J., Scattering of electromagnetic fields by a moving boundary: The one dimensional case, *IEEE Trans. Antennas Propag., AP-28*(6), 791–795, 1980.

Donelan, M. A., and W. J. Pierson, Jr., Radar scattering and equilibrium ranges in wind-generated waves with application to scatterometry, *J. Geophys. Res., 92*(C5), 4971–5029, 1987.

Harger, R. O., *Synthetic Aperture Radar Systems*, Academic, San Diego, Calif., 1970.

Harger, R. O., A fundamental model and efficient interference for SAR ocean imagery, *IEEE J. Oceanic Eng., OE-9*(4), 266–276, 1984.

Hasselmann, K., and M. Schieler, Doppler spectra of electromagnetic backscatter from the sea surface at centimeter-decimeter and decimeter wavelengths, Proceedings of the VIIIth Naval Hydrodynamics Symposium, *Rep. ACR-179*, pp. 361–388, Office of Naval Res. Dep. of the Navy, Arlington, Va., 1970.

Hasselmann, K., R. K. Raney, W. J. Plant, W. Alpers, R. A. Shuchman, D. R. Lyzenga, C. L. Rufenach, and M. J. Tucker, Theory of synthetic aperture radar ocean imaging: A MARSEN view, *J. Geophys. Res., 90*(C3), 4659–4686, 1985.

Ishimaru, A., *Wave Propagation and Scattering in Random Media*, 2 vols., Academic, San Diego, Calif., 1978.

Jain, A., SAR imaging of ocean waves: Theory, *IEEE J. Oceanic Eng., IE-6*(4), 13–139, 1981.

Jenkins, J. O., J. P. Randolph, D. G. Tilley, and C. A. Waters, The APL image processing laboratory, *APL Tech. Dig., 5*(1), 59–78, 1984.

Keller, W. C., and J. W. Wright, Microwave scattering and the straining of wind-generated waves, *Radio Sci., 10*(2), 139–147, 1975.

Kleinman, R. E., and R. B. Mack, Scattering by linearly vibrating objects, *IEEE Trans. Antennas Propag., AP-27*(3), 344–352, 1979.

Kodis, R. D., A note on the theory of scattering from an irregular surface, *IEEE Trans. Antennas Propag., AP-14*(1), 77–82, 1966.

Kwoh, D. S. W., and B. M. Lake, A deterministic, coherent, and dual-polarized laboratory study of microwave backscattering from water waves, I, Short gravity waves without wind, *IEEE J. Oceanic Eng., OE-9*(5), 291–308, 1984.

Longuet-Higgins, M. S., Reflection and refraction at a random moving surface, I, Pattern and paths of specular points, *J. Opt. Soc. Am., 50*(9), 838–844, 1960*a*.

Longuet-Higgins, M. S., Reflection and refraction at a random moving surface, II, Number of specular points in a Gaussian surface, *J. Opt. Soc. Am., 50*(9), 845–850, 1960*b*.

Longuet-Higgins, M. S., Reflection and refraction at a random moving surface, III, Frequency of twinkling in a Gaussian surface, *J. Opt. Soc. Am., 50*(9), 851–857, 1960*c*.

Longuet-Higgins, M. S., and R. W. Stewart, Radiation stresses in water waves: A physical discussion with applications, *Deep Sea Res., 11*, 529–562, 1964.

Lyzenga, D. R., R. A. Shuchman, J. D. Lyden, and C. L. Rufenach, SAR imaging of waves in water and ice: Evidence for velocity bunching, *J. Geophys. Res., 90*(C1), 1031–1036, 1985.

Phillips, O. M., *Dynamics of the Upper Ocean*, 2nd ed., Cambridge University Press, New York, 1977.

Plant, W. J., A relationship between wind stress and wave slope, *J. Geophys. Res., 87*(C3), 1961–1967, 1982.

Raney, R. K., Synthetic aperture imaging radar and moving targets, *IEEE Trans. Aerosp. Electron. Syst., AES-7*(3), 499–505, 1971.

Raney, R. K., SAR response to partially coherent phenomena, *IEEE Trans. Antennas Propag., AP-28*(6), 777–787, 1980.

Raney, R. K., and P. W. Vachon, Synthetic aperture radar imaging of ocean waves from an airborne platform: Focus and tracking issues, *J. Geophys. Res.*, in press, 1988.

Shemdin, O. H., et al., TOWARD experiment interim report, 2 vols., Jet Propul. Lab., Pasadena, Calif., 1986.

Shuchman, R. A., W. Rosenthal, J. D. Lyden, D. R. Lyzenga, E. S. Kasischke, H. Gunther, and H. Linne, Analysis of MARSEN *X* band SAR ocean wave data, *J. Geophys. Res., 88*(C14), 9757–9768, 1983.

Stogryn, A., Electromagnetic scattering from rough, finitely conducting surfaces, *Radio Sci., 2*(4), 415–428, 1967.

Swift, C. T., and L. R. Wilson, Synthetic aperture radar imaging of moving ocean waves, *IEEE Trans. Antennas Propag., AP-27*(6), 725–729, 1979.

Tomiyasu, K., Tutorial review of synthetic-aperture radar (SAR) with applications to imaging of the ocean surface, *Proc. IEEE, 66*(5), 563–583, 1978.

Tucker, M. J., The decorrelation time of microwave radar echoes from the sea surface, *Int. J. Remote Sens., 6*(7), 1075–1089, 1985.

Ulaby, F. T., R. K. Moore, and A. K. Fung, *Microwave Remote Sensing: Active and Passive*, vol. II, Addison-Wesley, Reading, Mass, 1982.

Valenzuela, G. R., Scattering of electromagnetic waves from a tilted slightly rough surface, *Radio Sci., 3*(11), 1057–1066, 1968.

Valenzuela, G. R., Theories for the interaction of electromagnetic and ocean waves—A review, *Boundary Layer Meteorol., 13*, 61–85, 1978.

Valenzuela, G. R., An asymptotic formulation for SAR images of the dynamical ocean surface, *Radio Sci., 15*, 105–114, 1980.

Wright, J. W., A new model for sea clutter, *IEEE Trans. Antennas Propag., AP-16*(2), 217–223, 1968.

K. Hasselmann, Max-Planck-Institut fuer Meteorologie, Bundesstrasse 55, 2000 Hamburg 13, Federal Republic of Germany.

D. P. Winebrenner, Polar Science Center, Applied Physics Laboratory, University of Washington, Seattle, WA 98195.

(Received December 14, 1987;
accepted February 10, 1988.)